CMB polarization with the Bicep and Keck experiments

Michael Crumrine

May 7, 2017

1 Introduction

1.1 A Brief History of Cosmology

The modern study of cosmology began in 1915 with Einstein's development of the general theory of Relativity [8]. By combining the Einstein Field Equations with the assumptions of a homogeneous and isotropic universe, Friedmann developed a cosmological model in 1922 which forms the core of the standard model of cosmology[10]. Hubble's observations in the 1930s showed an expanding universe[12] providing the first evidence for a Big Bang origin. This was further supported by the detection of the Cosmic Microwave Background by Penzias and Wilson in 1965[16].

1.2 The CMB and Inflation

The Cosmic Microwave Background (CMB) is colloquially called the "afterglow" of the Big bang and is the source of the oldest photons in the universe. Originally predicted by Alpher and Gamov in their description of Big Bang Nucleosynthesis as a consequence of the dense and hot early universe[1]. In the hot big bang, the early universe was an energetic plasma in which photons scattered continuously from free protons and electrons which prevented

propagation over large distances. Neutral Hydrogen was unstable in this period as most photons had energy well above the ionization threshold for Hydrogen. As the universe expanded, the temperature of this plasma decreased adiabatically until the free electrons and protons could combine to form stable, neutral Hydrogen. After this era of recombination about 380,000 years after the big bang, the photons decoupled from the plasma and began free streaming through the universe, redshifting due to continued expansion. We observe these photons today as a 2D "surface of last scattering" which follows the spectral distribution of a 2.73K blackbody.

Increasing experimental precision revealed a uniform CMB and isotropic universe on scales exceeding the size of the horizon predicted by Friedmann cosmological models. In 1981 Guth suggested a small period of exponential expansion to solve these two problems[11]. This theory of inflation has since seen further success in explaining the growth of cosmic structures as originating from quantum density fluctuations in the primordial projected to large scales by the inflationary epoch. Inflation also proposes an explanation for the lack of observed magnetic monopoles and other exotic relics that many grand unified theories (GUTs) predict would have been produced at the energy densities in the early universe. Any observable density of these exotic particles would have been heavily diluted by the exponential expansion of the inflationary epoch.

2   Science with the CMB

2.1   Mapping the CMB

Precision cosmology experiments have shown that the CMB is not truly uniform. Results from COBE in 1992[6] showed the nearly isotropic temperature spectrum of the CMB contains fluctuations on the order of 10 μK. These fluctuations correspond to density perturbations in the early universe. We examine the statistical distribution of these perturbations
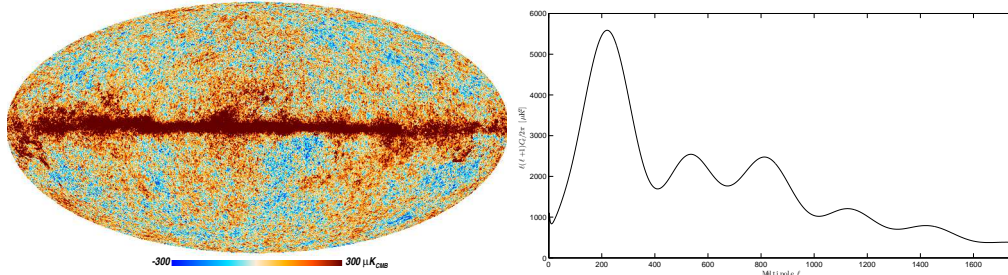
Figure 1: *Left:* The temperature power spectrum of the CMB. *Right:* A map of the temperature fluctuations in the CMB from Plank's 2015 results [19]. The primary and acoustic peaks in the temperature power spectrum can be used to constrain cosmological parameters that describe the geometry, evolution and composition of our universe.

with the spherical harmonics.

$$\delta T(\theta, \phi) = \sum_{m=-\ell}^{\ell} \sum_{\ell=0}^{\infty} a_{\ell m} Y_{\ell m}(\theta, \phi) \tag{1}$$

The isotropy of the universe prevents the prediction of any individual $a_{\ell m}$. We therefore take an average over m to form the angular power spectrum C_ℓ.

$$C_\ell = \frac{1}{2\ell + 1} \sum_{m=-\ell}^{\ell} |a_{\ell m}|^2 \tag{2}$$

Figure 1 shows the fluctuations in the temperature spectrum of the CMB as observed by the Planck experiment in their 100 GHz band and the corresponding angular power spectrum of these fluctuations. The relative sizes and locations of the peaks in this power spectrum can help constrain cosmological parameters that describe the composition and evolution of our universe.

2.2 Polarization Anisotropies

In addition to the temperature anisotropies CMB photons are partially polarized due to Thompson scattering in a non-uniform temperature field. This CMB polarization was predicted at the $\approx 10\%$ level by Bond et al [7] and first detected by DASI in 2002 [14]. Polnarev

[21] realized that an inflationary period would imprint an additional polarization signal on the CMB due to the production of gravitational waves during the inflationary epoch. The spatial expansion and compression resulting from a passing gravitational wave would produce a sufficient temperature quadrupole to impart an additional net polarization on the CMB photons.

This inflationary gravitational wave (IGW) signal is expected to be orders of magnitude fainter than the signal due to the temperature fluctuations in the primordial plasma and difficult to separate in the Stokes parameter space conventionally used when studying linearly polarized light. It was shown by Kamionkowski et al [13] that the polarization could instead be parameterized by a gradient (E-mode) and curl (B-mode) component. The polarization component due to temperature quadrupoles in the primordial plasma naturally follows the temperature gradients of the plasma and so produces the E-mode component. The tensor perturbations due to passing gravitational waves are not restricted in this way and can therefore create both E-modes and B-modes. The amplitude of this B-mode signal is characterised by the energy scale of inflation and related to the E-mode polarization signal by the tensor to scalar ratio r. Figure 2 shows the theoretical power spectra of CMB perturbations in the ΛCDM standard model of Cosmology with the addition of an $r = 0.1$ IGW B-mode signal.

As previously mentioned the E, B parameter space is preferred for analyzing the polarization signal in the CMB as it provides a direct method for extracting the signal due to inflationary gravitational waves. However, the Bicep / Keck detectors generate maps in the Stokes Q, U parameter space. By performing a transformation in Fourier space we can convert Stokes Q and U polarization into the desired E-mode and B-mode parameter space.

2.3   Gravitational Lensing

Although the mean free path of CMB photons is effectively infinite, the presence of large scale structures in our universe can interact with these photons and alter the signals we

detect in the CMB. In particular, gravitational lensing due to high matter concentrations is capable of converting some E-modes into B-modes by relocating polarized photons on the sky. The transformation from Q and U to E and B occurs in Fourier space and is inherently nonlocal. The relocation of polarized photons by a gravitational lens is therefore capable of converting E modes to B modes. Figure 2 also shows lensing contribution to the B-mode angular power spectrum. The lensing contribution to the B-mode spectrum is largest at small scales due to the high matter densities which produce strong gravitational lenses. We note also that in principle gravitational lensing is capable of converting B-modes to E-modes, however the significantly higher amplitude of the E-mode signal is not highly effected by the addition of this small signal.
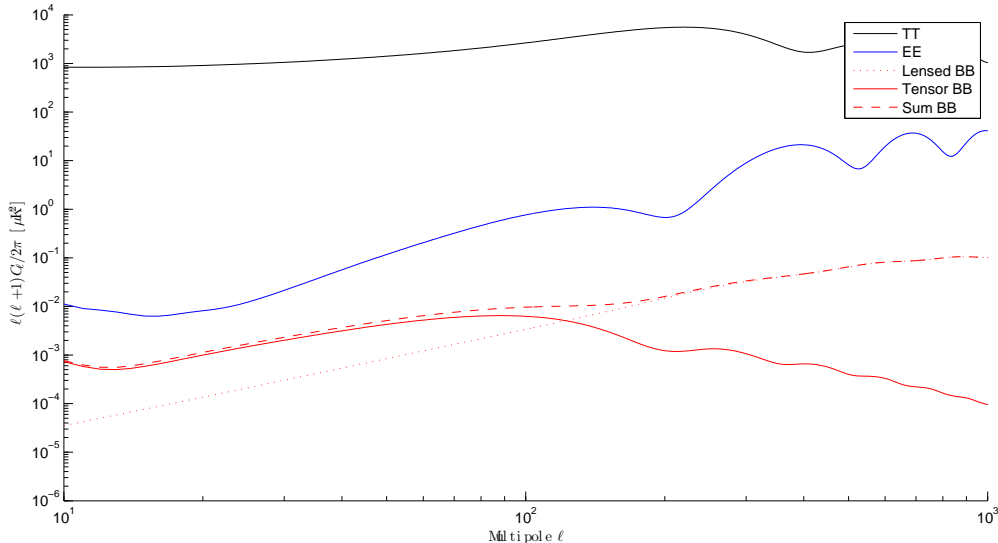

Figure 2: The CMB power spectrum of the ΛCDM standard model of cosmology as calculated by CAMB using parameters from Planck 2013. The temperature anisotropies (black) contain orders of magnitude more power than the E-mode (blue) and B-mode (red) polarization anisotropies. The BB spectrum is split into a lensing component (dotted) and a tensor component (solid) plotted at the $r = 0.1$ level. Current constraints on IGWs constrain the signal at less than the $r = 0.1$ level shown here. We note that some inflationary models predict a tensor to scalar ratio that is unobservably small.
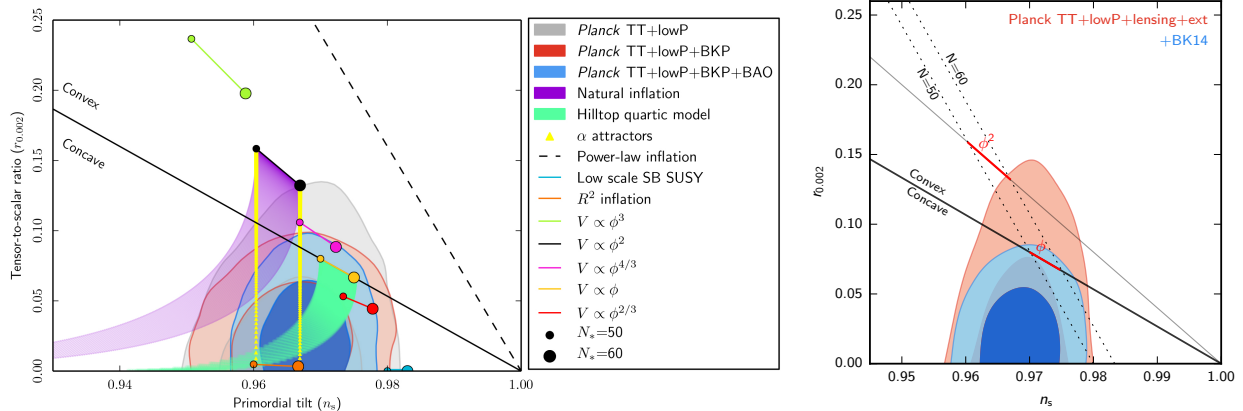
Figure 3: Left: Reproduced from Planck 2015 XX: "Constraints on Inflation"[20] shows theoretical predictions for select inflationary models in the n_s,r parameter space and current constraints on those parameters. The two dots correspond to different numbers of e-folds. Right: Reproduced from BK-VI [4] showing improved constraints in this parameter space from the latest Bicep / Keck data including a 95GHz band.

2.4 Constraints on Inflation

Although the theory of inflation provides an attractive solution to a number of problems with the standard big bang cosmology, the exact physics of inflation are still undetermined. The favored theory of slow roll inflation proposes a scalar field ϕ in which the potential of the field dominates over its kinetic energy. There mare many possible potentials which fit the mathematical requirements of inflation theory which yield a range of values for the tensor to scalar ratio r. By continuing to push the constraints on r we restrict the possible potentials of this scalar field. A summary of current restrictions on inflation in the r and n_s parameter space shown in Figure 3. The Bicep / Keck constraints heavily disfavor the ϕ^2 model but still allow for other models which have $r < 0.1$

3 The Bicep and Keck Program

The Bicep/Keck experiments are a staged series of small aperture ground based telescopes which aim to produce extremely deep degree-scale polarization maps of the CMB. The high systematics control and long integration time have enabled Bicep and Keck to set the strictest
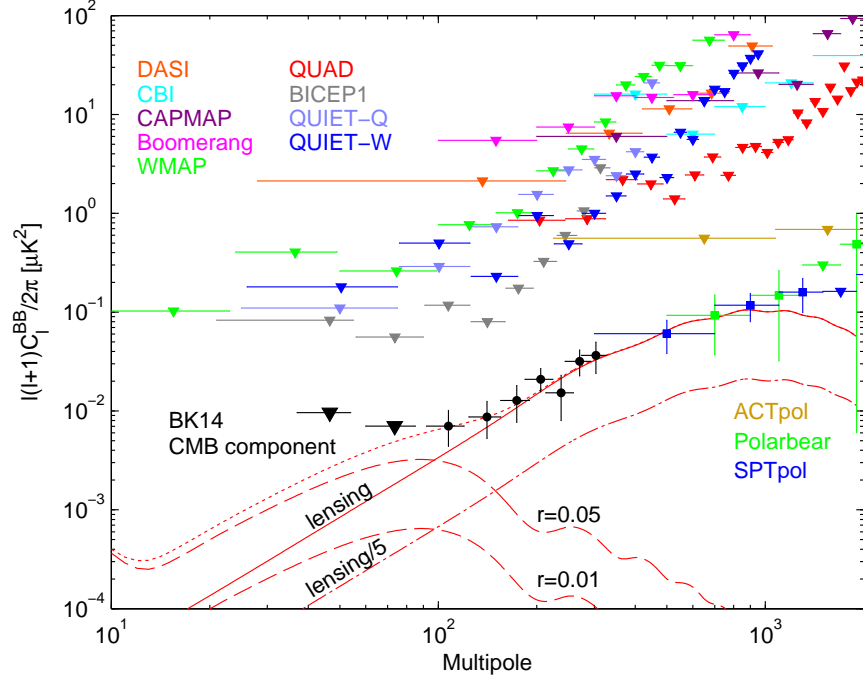
Figure 4: Published B-mode polarization measurements of the CMB. Theoretical predictions for lensing B-modes (solid red) and IGW B-modes (dashed red) for two values of r are shown. The SPTpol, Polarbear and Bicep/Keck experiments have all recently detected the B-mode lensing signal. Bicep and Keck are currently alone in probing large angular scales for the IGW B-mode signal

limits on inflationary gravitational wave B-mode signals to date. Figure 4 shows current published measurements of B-mode polarization in the CMB. The Bicep and Keck experiments along with SPTpol and Polarbear have measured the B-mode component due to lensing at high significance. Bicep and Keck have currently published the strictest constraints on B-mode measurements on large angular scales.

Each generation of receiver builds on the experience gained from the previous generation while pushing deeper in sensitivity. Bicep1 was deployed to the south pole in 2006 and used 98 feedhorn coupled bolometers observing at 100GHz and 150GHz. After observing for three seasons, Bicep1 established the leading upper bounds on inflation at $r < 0.70$ [2]. The strategies developed for observation, calibration and systematics control during the operation of Bicep1 proved the efficacy of small aperture refractors for CMB polarization studies and have enabled the high systematics control achieved by subsequent experiments in the series.

Building on the techniques developed with its predecessor, Bicep2 replaced Bicep1 in 2009. It exchanged feedhorn coupled bolometers for antenna-coupled transition edge sensor (TES) bolometer arrays developed at JPL which have been used in every subsequent experiment in the series. Concentrating its observing power at 150GHz, in March 2014 Bicep2 announced a detection of excess signal in its observing band consistent with an IGW signal of $r = 0.2$[3]. However, the interpretation of this excess as IGW signal relied heavily on models of polarized dust emission. Later that year new high frequency maps from the Planck experiment indicated that the dust models had underestimated polarized emission in the faintest sky regions [17] including the Bicep / Keck observing patch. A subsequent joint analysis with Planck and cross correlation between the Planck 353GHz and Bicep2 150GHz maps showed that a substantial part of the observed excess in Bicep2 was due to polarized dust emissions [5]. Using the new maps of polarized dust provided by Planck, this joint analysis established a new upper limit of $r < 0.12$ [5].

The Keck Array deployed to the south pole in 2012 with five 150GHz receivers similar to Bicep2. These additional receivers confirmed the excess signal found with Bicep2 and contributed to the March 2014 results. In addition to extending the Bicep2 survey depth at 150GHz the Keck array has extended observations into three other observing bands at 95GHz, 220GHz and 270GHz. This extension into other frequencies harnesses the Bicep/Keck program's proven capability to make deep maps in order to further constrain galactic foregrounds and refine the models of polarized dust emission. The Keck array is in its final observing season with four receivers in the 220GHz band and one at 270GHz.

In the fall of 2014 Bicep3 was deployed at the south pole to run concurrently with the Keck array. Bicep3 vastly expands the design of the Bicep2 instrument with a a larger focal plane with an order of magnitude more detectors and an aperture twice the size of the Bicep2 receiver. Just as Bicep2 was expanded into the five receiver Keck array, Bicep3 serves as our pathfinder instrument leading to the eventual replacement of the Keck array with the Bicep
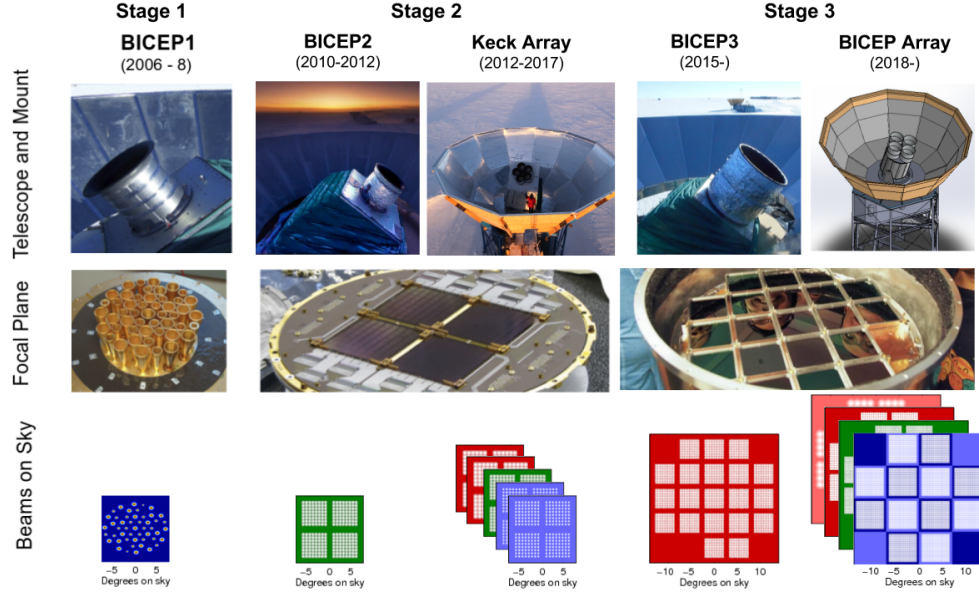
Figure 5: The progression of the Bicep/Keck program from Bicep1 to Bicep Array. The bottom row shows the beam patterns of the focal planes on the sky. With the exception of Bicep1 the focal plane colors correspond to band centers of: 35GHz - pink, 95GHz - red, 150GHz - green, 220 GHz - light blue, 270GHz - dark blue.

array.

The Bicep array is a funded experiment which will replace the Keck Array for multifrequency observations. Using the more powerful Bicep3 style receivers, Bicep array will field four receivers: one each centered at 95GHz and 150GHz, and two dual band 35/40GHz and 220/270GHz receivers. The new 35/40GHz band will heavily constrain galactic synchrotron radiation, the upper limits of which are currently set by WMAP's 23GHZ band and cross correlation with our own 95GHz band. The addition of the 95GHz and 150GHz receivers will continue to push sensitivity in the frequencies at which foreground contributions are expected to be faintest and at the Bicep / Keck maps are already the deepest. The final high frequency receiver will continue the Keck array's work in constraining emissions from polarized galactic dust. Directly observing these foregrounds in our own observing patch eliminates the need to account for spatial variation of the foreground spectra.
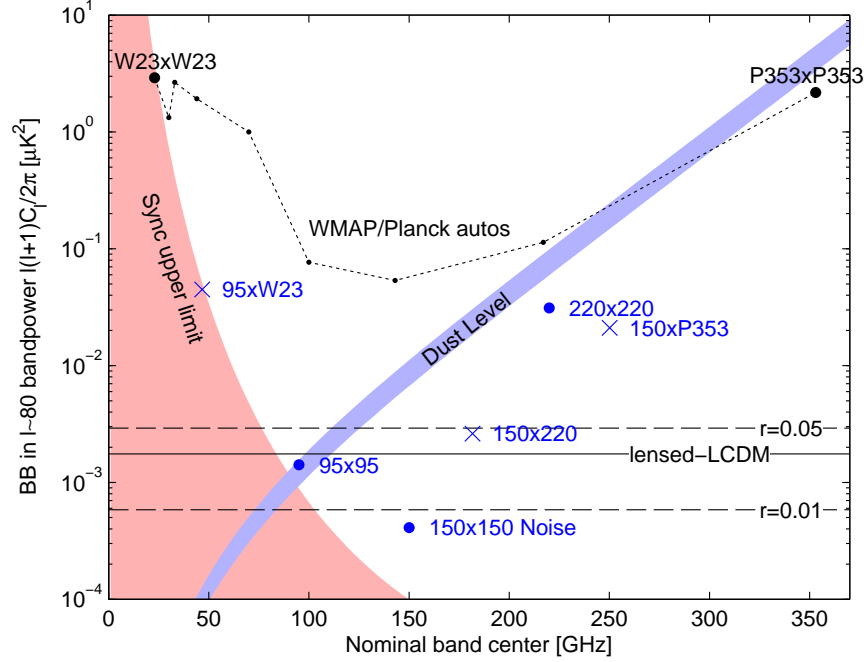
Figure 6: Noise levels in the Bicep/Keck combined observations through the 2015 observing season. The shaded regions show constraints on the signal level of galactic foregrounds and signal levels corresponding to select values of r are shown at the bottom. All values are shown in the $\ell = 80$ bandpower where the IGW signal is expected to be maximal (See Figure 2.)

4 Multifrequency Observations

CMB polarization experiments must be able to separate polarized foreground signals from those imprinted on the CMB. Although these signals can be minimized by selection of observing area their emissions must be constrained and accounted for. As shown by the 2014 joint analysis between Bicep2/Keck and Planck, constraints on these models have significant impact on the interpretation of any observed excess signal. By expanding observations into multiple frequencies, the Keck array has begun to constrain these dust emissions as well as emissions due to galactic synchrotron as shown in Figure 6.

4.1 Polarized Dust

Polarized emissions from galactic dust provide an excess BB signal on top of that expected from ΛCDM and gravitational lensing. These emissions are strongly frequency dependent and exhibit a power law like behavior. As shown in Planck XXII [18] the spectral energy distribution of galactic dust can be described by a modified blackbody spectrum

$$I_d = A_d \nu^\beta B_\nu(T_d) \tag{3}$$

Where A_d sets the amplitude at a chosen frequency, $\beta_d > 0$ is the spectral index of dust emission and $B_\nu(T)$ is the standard blackbody spectrum. In order to fully constrain the dust signal we must complement this intensity spectrum with a description of the dust's power spectral behavior.

$$D_\ell \propto \ell^\alpha \tag{4}$$

where $D_\ell = C_\ell \frac{\ell(\ell+1)}{2\pi}$. The parameters in these equations model the dust contribution to polarization signal in our field. As Equation 3 shows this signal is brighter at higher frequencies. Our current constraints use the Planck 353GHz maps and cross correlation with our own 220GHz maps to set these dust parameters and extrapolate to our 95GHz and 150GHz bands. This necessarily means that any uncertainty contained in the high frequency observations is magnified due to the lever arm in frequency.

Figure 6 shows the noise uncertainty and signal levels the $\ell = 80$ bandpower where the IGW signal is expected to peak. We are able to detect signal in excess of that predicted by ΛCDM with high significance in our 150GHz band due to the low noise level. However, the high P353GHz noise as compared to dust signal does not provide significant enough constraining power to separate dust signal from potential IGW signal in the 150GHz band. The 220x220 point shows preliminary numbers from our 2015 observing season in which the

Keck array operated with two 220GHz receivers and provides similar constraining power to the Planck 353GHz data while being closer to our deepest observing bands. Two additional 220GHz receivers were added for the 2016 observing season and observations at 270GHz will begin in the current 2017 season. These observations will allow us to produce continually improving constraints on dust in our field.

4.2   Galactic Synchrotron

At low frequencies we must account for polarized galactic synchrotron emissions. An upper limit for this signal is shown in Figure 6. Rather than increasing in intensity at higher frequencies, galactic synchrotron contributions are strongest at low frequencies. We model synchrotron emission intensity as

$$I_\nu = A_s \nu^{\beta_s} \tag{5}$$

where $\beta_s < 0$ describes the fall off in intensity with frequency and A_s is the amplitude. The angular power spectrum of galactic synchrotron follows the same form as dust (Equation 4). The points shown in Figure 6 mark the upper limit of synchrotron emissions as the noise level of current observations in these bands is not sufficient for detection. Models of the contribution due to synchrotron do not predict significant contamination at frequencies upwards of 150GHz due to the strong frequency dependence.

5   Bicep Array

5.1   Experiment Overview

Bicep Array will deploy four Bicep3 style receivers in four frequency bands with first light expected in 2019. Building on the success of previous experiments, Bicep Array will continue to use the antenna coupled transition edge sensor (TES) bolometers developed by JPL.

These detectors leverage the strong temperature-dependence of superconductors near their transition temperature to detect extremely faint signals. Each pixel is composed of two detectors which are sensitive to orthogonal linear polarizations. By co-locating these detectors we can use the pair sum to generate intensity maps corresponding to the CMB temperature and the pair difference to generate the Stokes Q and U maps.

Each Bicep array receiver will field ≈ 10 time the detectors of a Keck receiver in the same band. With the additional increase in aperture from 26cm to 55cm we will quickly push sensitivity to synchrotron with Bicep Array's new band and continue to push sensitivity in our deepest 95GHz and 150GHz bands. Established sensitivities and future projections for the sensitivity of the Bicep / Keck experiments including the Bicep array are shown in Figure 7. As we continue to increase in sensitivity to r, the B-mode lensing component will become a significant contributor to σ_r. This achromatic foreground cannot be constrained with multifrequency observations but it can be accounted for via delensing. Given a high resolution map of the angular deflection field $\Delta\phi$ of the CMB photons from last scattering to observation it is possible to undeflect Stokes Q, U maps of polarized signal and so "delense" the polarization signal. The third generation SPT-3G receiver deployed to the South Pole in late 2016 and will spend a significant fraction of their time observing the Bicep/Keck sky patch to aid the delensing effort. In collaboration with SPT-3G we expect to achiever $\sigma_r < 0.005$ by the end of the decade.

5.2 Cryogenic Considerations

The cryogenic operating temperatures of our detector and optics system require a specially designed housing to thermally isolate the focal plane. As with Keck and Bicep3 the Bicep Array cryostats will consist of 3 nested concentric shells: an ambient temperature vacuum jacket, an intermediate radiation shield, and a cold optics tube. Hereafter we refer to these individual stages by their nominal operating temperatures of 300K, 50K and 4K respectively.
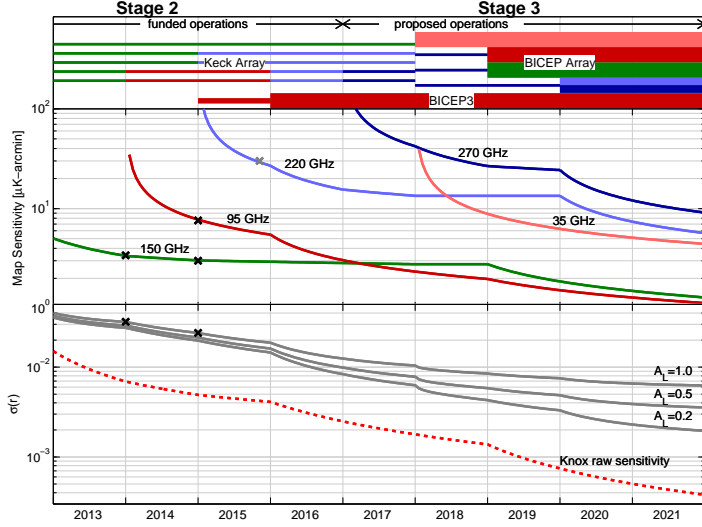
Figure 7: Projected sensitivity of the ongoing and planned Bicep/Keck observational program. The increased throughput of the Bicep array receivers will provide increased sensitivity and continue to constrain inflation at a rapid rate. *Note: Projections are directly scaled from published results and thus include real-world inefficiencies that are not reflected in purely theoretical projections. X's mark sensitivities achieved in BKP and BK-VI [4, 5].* Middle: Map depth at each frequency as a function of time. Bottom: Sensitivity to r for selected levels of delensing efficiency. Performance between $A_L = [0.2, 0.5]$ is expected.

This nested approach protects the low temperature optics from absorbing significant radiative power as $P \propto T^4$. In addition to radiation shielding, there is an additional trade-off between structural support and heat conduction between the temperature shells. A low conductive loading may introduce significant deviation in pointing direction while a more structural support system may increase the thermal load on the cooling system.

5.3   Thermal Loading

The cryostat is operated at high vacuum ($\approx 10^{-5}$mTorr) which largely eliminates conductive loading due to residual gasses. The two largest contributions are then due to conduction across the structural supports and radiation from higher temperature stages. Of these, the radiation absorbed by the lower temperature shells has the highest possible contribution. Radiative heat transfer for cryogenic systems is a well studied subject. We follow Ekin's textbook [9] on cryogenic engineering to estimate this thermal load according to:

$$\dot{Q}_{h \to c} = \sigma A_c E(T_h^4 - T_c^4) \tag{6}$$

where the h and c subscripts denote the hot and cold surfaces respectively, and E depends on the emissivity of the surfaces as

$$E = \frac{1}{1/\epsilon_h + 1/\epsilon_c - 1} \tag{7}$$

Equation 6 is valid for parallel plates, and concentric cylinders assuming the specular reflection regime. Table 1 shows typical emissivities for the materials used in the Bicep Array cryostats. In addition to the radiative load, the structural supports conduct heat between the temperature shells according to the Fourier heat transfer law:

$$\dot{Q}_{1 \to 2} = \int_{T_1}^{T_2} \frac{A}{L} K(T) dT \tag{8}$$

The large temperature change across the support struts require a detailed knowledge of how the materials' thermal conductivity changes with temperature. NIST maintains a collection of thermal conductivity measurements for commonly used materials in cryogenic design including Aluminum and Titanium [15]. Bicep Array uses six Titanium "V" shaped supports at the front end to maintain concentricity of the optics tube and twelve carbon fiber struts at the back end which support most of the weight. Carbon fiber as a material is non-standardized which makes determining the thermal properties difficult, especially at high temperatures where few conductivity measurements exist. We therefore supplement published low temperature measurements with direct measurements of conducted power in a test cryostat system.

Material	Emissivity
Rough Aluminum	$\epsilon = 0.07 - 0.1$
Polished Aluminum	$\epsilon = 0.04 - 0.06$
Aluminized Mylar	$\epsilon = 0.035$
OFHC Copper	$\epsilon = 0.65$

Table 1: Typical emissivity values for materials used in the construction of the Bicep Array cryostats.

5.4   Radiation Shielding

The large surface area of the 50K radiation shield absorbs a significant amount of power. Using Equation 6 the raw radiated heat transfer to the 50K shell from the enclosing 300K vacuum jacket is 86.13W which is far outside the capacity of our fist stage pulse tube cooling system. To reduce this load we surround the lower temperature shell with a series of thermally floating layers of Aluminized Mylar. This multiple layer insulation (MLI) creates a temperature gradient of isolated radiating shells which significantly reduces the transmitted power by reducing the $\Delta(T^4)$ term of Equation 6. The modified power transmission to the cold shell when shielded by N layers of MLI is

$$\dot{Q}_{h \to c} = \frac{\sigma A_c (T_h^4 - T_c^4)}{1/\epsilon_h + 1/\epsilon_c - 1 + N(2/\epsilon_m - 1)} \tag{9}$$

where ϵ_m is the emissivity of the MLI. Placing 30 thermally floating layers in between the 300K vacuum shell and the 50K radiation shield reduces absorbed radiative power to 0.96W at which point it becomes subdominant to the thermal loading from the structural supports and the absorptive optical filters. Although the radiation absorbed by the 4K stage from the 50K stage is much lower due to the smaller $\Delta(T^4)$ we choose to include 5 layers of MLI between the 50K radiation shield and the 4K optics tube as well.

	50K	4k
Radiation	2.73W	0.0479W
Bottom Supports	< 2.4W	0.0759W
Top Supports	1.93W	0.0821W
Data Cables	1.07W	0.05W
Optical Filters	12.51W	0.1538W
Total	20.64W	0.4097W

Figure 8: Above we show the calculated thermal load on the 50K radiation shield and the 4K optics tube due to radiation from higher temperature stages, conduction across the structural supports, conduction across the data cables and radiation absorbed by the optical filters. The upper limit for power conducted across the bottom supports to the 50K radiation shield is set by observed performance of the Keck receivers. Note that the radiation numbers shown here include power absorbed by all parts of the corresponding temperature stages and include absorption from flanges which do not have sufficient clearance for an MLI blanket.

5.5   Thermal Performance

Using the equations above we can estimate the thermal loading on each of the two cryogenic stages of the cryostat and estimate an operating temperature for both stages of our pulse tube cooling system. We require a 4K stage operating temperature of less than $\approx 3.5K$ to allow the second stage He fridge to function. The 50K stage operating temperature is not as crucial, however we thermally sink optical filters to the 50K radiation shield. Lower temperatures then allow for cooler optical filters which radiate less power directly down the optics tube. Using equations 8 and 9 we calculate the thermal load onto the 4K and 50K stages as shown below in Table 8.

In addition to the thermal load due to radiation from higher temperature stages and conduction across the structural supports we also account for conduction across the data cables which read out our detectors and the radiation absorbed by our optical filters at each stage. The thermal load due to the optical filters is obtained using data from the Bicep3 experiment's actual performance. We expect similar performance from Bicep Array which shares the same aperture size and filtering scheme as Bicep3.

Using these numbers we can estimate the operating temperature of our pulse tube system by comparing the thermal load with the capacity curve supplied by the manufacturer shown
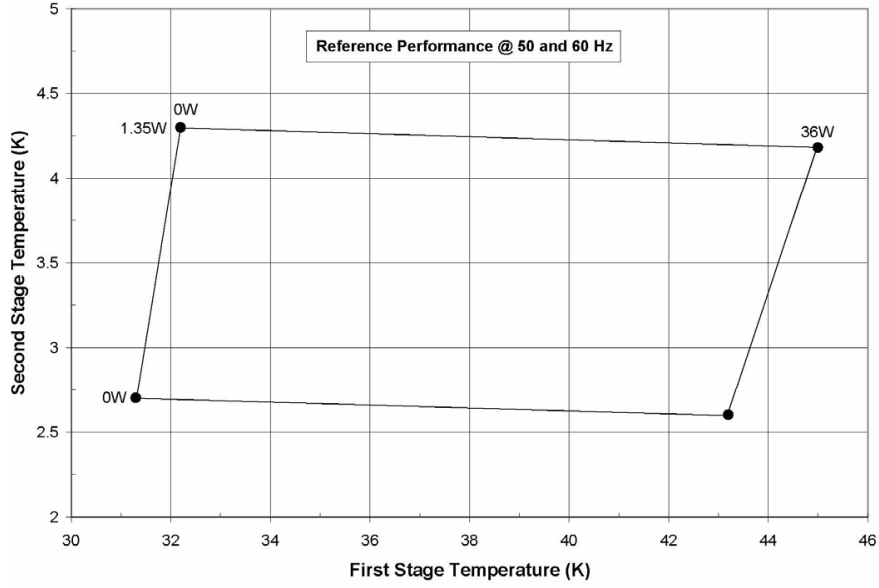
Figure 9: Reference capacity curve for the PT415 Pulse Tube Cryocooler with remote motor option as supplied by Cryomech. The four data points show the incident power applied to the first stage (top) and second stage (left). Using these points as a reference we can estimate the operating temperature of the two pulse tube stages once we have calculated the thermal load on each stage. The first stage and second stage of this pulse tube cooling system are connected to our 50K radiation shield and 4K optics tube respectively. Using the estimated thermal load from Table 8 gives an operating temperature of 39K for the first stage and 3.2K for the second stage. The Bicep3 pulse tube is observed to significantly outperform the Cryomech standard.

in Figure 9. This capacity curve shows the expected operating temperature of pulse tube's first and second stages - connected to our 50K radiation shield and 4K optics tube respectively - given the incident power on both stages. The calculated thermal load suggests a first stage operating temperature of 39K and a second stage temperature of 3.2K. While this is sufficient for operation, there is not much margin. We note however that the Bicep3 pulsetube is oberved to significantly outperform the Cryomech standard by ≈ 50% on the first stage. This extra cooling capacity will help to alleviate some of the loading onto the optics stage by reducing the power transferred to the 4K optics tube.
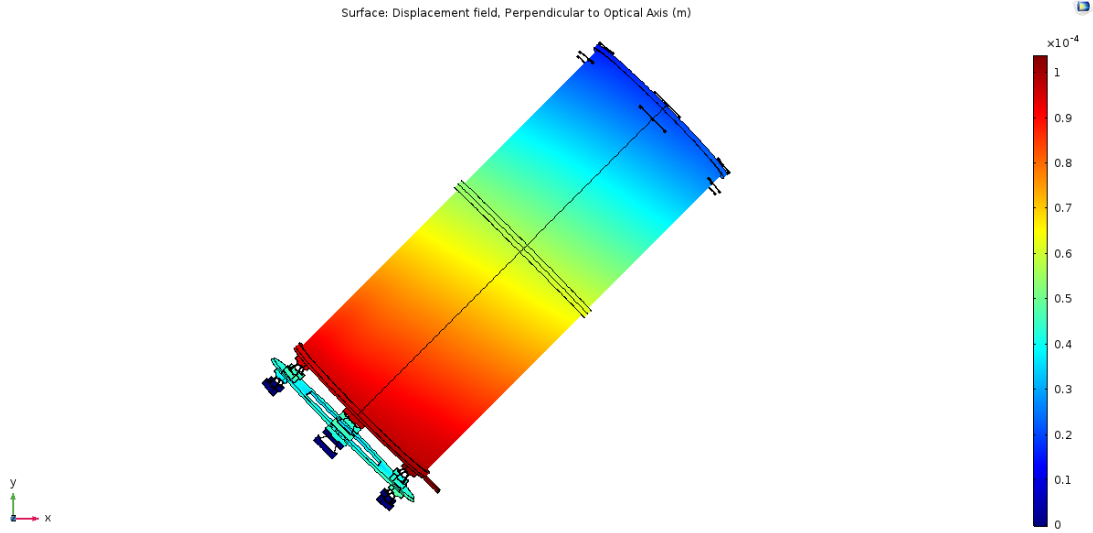
Figure 10: Simulation results of the deformation of the 4K optics tube under gravitational load as calculated by the COMSOL simulation suite. The colorscale shows the magnitude of deformation in the vector direction perpendicular to the optical axis (ie: -45 degrees). The deflections of the 50K radiation shield to which the 4K optics tube is attached are included in this simulation, however the shield is hidden for clarity.

5.6 Implications for Pointing

The thermal load is closely tied to the pointing accuracy of the receiver. Table 8 shows that heat conduction across the supports is subdominant only to the thermal load from the optical filters. However, if we wish to reduce the conductive load across these supports it comes at the cost of a less rigid support system. To estimate the pointing accuracy of our optics tube, we use finite element analysis to simulate the deformations of the cryostat under gravitational load. Figure 10 shows the results of a structural simulation performed with the COMSOL Multiphysics software suite. In this simulation the cryostat is rotated to our lowest observing elevation of 45 degrees and the gravitational load of all interior components are attached to their respective mounting surfaces.

We are most interested in the deformations of the cryostat in the direction perpendicular to the optical axis. This will give an indication of the shift in pointing of the optics tube with respect to the fixed outer vacuum jacket. A simple calculation of the deflection of the

19

back of the optics tube with respect to the front yields a pointing shift of 10 arcseconds along the tube's 1.65m length. As a secondary check, we also fit a plane to three points on the deformed plate that supports our focal plane and calculate the angle of the surface normal to be 45.0028 degrees from the horizontal corresponding to a 10.255 arcsecond pointing shift. The detectors used in Bicep Array will have large beam sizes compared to this shift with the 270GHz detectors having the smallest beams of 9 arcmin FHWM. This pointing shift is then acceptable for the Bicep array experiment.

6   Conclusions

The Bicep Array experiment will continue the successful achievements of its predecessors by pursuing increasingly deep maps of the polarized component of the CMB and expanding these observations into other frequencies in order to constrain galactic foregrounds. The design of the cryostat is nearing completion and delivery of the first receiver is expected during the fall of 2017. After careful integration and characterization of the detectors and readout systems Bicep Array will deploy its first receiver to the South Pole in the winter of 2018. With a dual band 35/40 GHz focal plane this first receiver will rapidly push down the upper limits on polarized emission from galactic synchrotron. Future receivers will continue to push sensitivity in the bands at which Bicep / Keck have the deepest maps and at which contribution from galactic foregrounds are dimmest. With delensing in conjunction with SPT-3G we expect to reach a sensitivity of $\sigma_r < 0.005$ by the end of the decade. This will place significant constraints on inflationary models and the dynamics of the universe's evolution within the first instants after the big bang.

References

[1] R. A. Alpher, H. Bethe, and G. Gamow. "The Origin of Chemical Elements". In: *Physical Review* 73 (Apr. 1948), pp. 803–804. DOI: `10.1103/PhysRev.73.803`.

[2] D. Barkats et al. "Degree-scale Cosmic Microwave Background Polarization Measurements from Three Years of BICEP1 Data". In: *apj* 783, 67 (Mar. 2014), p. 67. DOI: `10.1088/0004-637X/783/2/67`. arXiv: `1310.1422`.

[3] BICEP2 Collaboration et al. "Detection of B-Mode Polarization at Degree Angular Scales by BICEP2". In: *Physical Review Letters* 112.24, 241101 (June 2014), p. 241101. DOI: `10.1103/PhysRevLett.112.241101`. arXiv: `1403.3985`.

[4] BICEP2 Collaboration et al. "Improved Constraints on Cosmology and Foregrounds from BICEP2 and Keck Array Cosmic Microwave Background Data with Inclusion of 95 GHz Band". In: *Physical Review Letters* 116.3, 031302 (Jan. 2016), p. 031302. DOI: `10.1103/PhysRevLett.116.031302`. arXiv: `1510.09217`.

[5] BICEP2/Keck and Planck Collaborations et al. "Joint Analysis of BICEP2/Keck Array and Planck Data". In: *Physical Review Letters* 114.10, 101301 (Mar. 2015), p. 101301. DOI: `10.1103/PhysRevLett.114.101301`. arXiv: `1502.00612`.

[6] N. W. Boggess et al. "The COBE mission - Its design and performance two years after launch". In: *apj* 397 (Oct. 1992), pp. 420–429. DOI: `10.1086/171797`.

[7] J. R. Bond and G. Efstathiou. "Cosmic background radiation anisotropies in universes dominated by nonbaryonic dark matter". In: *apjl* 285 (Oct. 1984), pp. L45–L48. DOI: `10.1086/184362`.

[8] A. Einstein. "Die Feldgleichungen der Gravitation". In: *Sitzungsberichte der Königlich Preußischen Akademie der Wissenschaften (Berlin), Seite 844-847.* (1915).

[9] J. W. Ekin. *Experimental techniques for low-temperature measurements: cryostat design, material properties, and superconductor critical-current testing.* Oxford University Press, 2006.

[10] A. Friedmann. "Über die Krümmung des Raumes". In: *Zeitschrift fur Physik* 10 (1922), pp. 377–386. DOI: 10.1007/BF01332580.

[11] A. H. Guth. "Inflationary universe: A possible solution to the horizon and flatness problems". In: *prd* 23 (Jan. 1981), pp. 347–356. DOI: 10.1103/PhysRevD.23.347.

[12] E. Hubble. "A Relation between Distance and Radial Velocity among Extra-Galactic Nebulae". In: *Proceedings of the National Academy of Science* 15 (Mar. 1929), pp. 168–173. DOI: 10.1073/pnas.15.3.168.

[13] M. Kamionkowski, A. Kosowsky, and A. Stebbins. "A Probe of Primordial Gravity Waves and Vorticity". In: *Physical Review Letters* 78 (Mar. 1997), pp. 2058–2061. DOI: 10.1103/PhysRevLett.78.2058. eprint: astro-ph/9609132.

[14] J. M. Kovac et al. "Detection of polarization in the cosmic microwave background using DASI". In: *nat* 420 (Dec. 2002), pp. 772–787. DOI: 10.1038/nature01269. eprint: astro-ph/0209478.

[15] *National Institute of Standards and Technology: Materials Measurement Laboratory - Cryogenic Technologies Group.* http://cryogenics.nist.gov.

[16] A. A. Penzias and R. W. Wilson. "A Measurement of Excess Antenna Temperature at 4080 Mc/s." In: *apj* 142 (July 1965), pp. 419–421. DOI: 10.1086/148307.

[17] Planck Collaboration et al. "Planck intermediate results. XIX. An overview of the polarized thermal emission from Galactic dust". In: *aap* 576, A104 (Apr. 2015), A104. DOI: 10.1051/0004-6361/201424082. arXiv: 1405.0871.

[18]   Planck Collaboration et al. "Planck intermediate results. XXII. Frequency dependence of thermal emission from Galactic dust in intensity and polarization". In: *aap* 576, A107 (Apr. 2015), A107. DOI: 10.1051/0004-6361/201424088. arXiv: 1405.0874.

[19]   Planck Collaboration et al. "Planck 2015 results. VIII. High Frequency Instrument data processing: Calibration and maps". In: *aap* 594, A8 (Sept. 2016), A8. DOI: 10.1051/0004-6361/201525820. arXiv: 1502.01587.

[20]   Planck Collaboration et al. "Planck 2015 results. XX. Constraints on inflation". In: *aap* 594, A20 (Sept. 2016), A20. DOI: 10.1051/0004-6361/201525898. arXiv: 1502.02114.

[21]   A. G. Polnarev. "Polarization and anisotropy induced in the microwave background by cosmological gravitational waves". In: *azh* 62 (Dec. 1985), pp. 1041–1052.